Multiple control of few-layer Janus MoSSe systems

Shuanglong Liu [1,2] James N. Fry [1] and Hai-Ping Cheng [1,2,3,*]
[1]*Department of Physics, University of Florida, Gainesville, Florida 32611, USA*
[2]*Quantum Theory Project, University of Florida, Gainesville, Florida 32611, USA*
[3]*Center for Molecular Magnetic Quantum Materials, University of Florida, Gainesville, Florida 32611, USA*

(Received 24 November 2020; revised 2 June 2021; accepted 9 June 2021; published 24 June 2021)

In this computational work based on density functional theory, we study the electronic and electron transport properties of asymmetric multilayer MoSSe junctions, known as Janus junctions. Focusing on four-layer systems, we investigate the influence of electric field, electrostatic doping, strain, and interlayer stacking on the electronic structure. We discover that a metal-to-semiconductor transition can be induced by an out-of-plane electric field. The critical electric field for such a transition can be reduced by in-plane biaxial compressive strain. Due to an intrinsic electric field, a four-layer MoSSe can rectify out-of-plane electric current. The rectifying ratio reaches 34.1 in a model junction Zr/four-layer MoSSe/Zr and can be further enhanced by increasing the number of MoSSe layers. In addition, we show a drastic sudden vertical compression of four-layer MoSSe due to in-plane biaxial tensile strain, indicating a second phase transition. Furthermore, an odd-even effect on electron transmission at the Fermi energy for Zr/n-layer MoSSe/Zr junctions with $n = 1, 2, 3, \ldots, 10$ is observed. These findings reveal the richness of physics in this asymmetric system, and they strongly suggest that the properties of four-layer MoSSe are highly tunable, thus providing a guide to future experiments relating to materials research and nanoelectronics.

DOI: 10.1103/PhysRevMaterials.5.064007

I. INTRODUCTION

Two-dimensional (2D) transition-metal dichalcogenides (TMDs) have potential applications in electronics/optoelectronics [1,2] due to the presence of a direct band gap and sufficiently high mobility. The computed band gaps of TMDs vary by ∼2 eV, depending on the chemical composition [3], which provides rich opportunities for different applications. In 2017, a semiconducting Janus transition-metal dichalcogenide MoSSe was synthesized in experiments independently by Zhang *et al.* [4] and by Lu *et al.* [5], where one face of MoSSe consists of S atoms and the other consists of Se atoms. This discovery has inspired a surge of research into Janus 2D materials, including but not limited to MoSSe [6–16]. For example, superior charge carrier mobility was predicted in monolayer WSSe [6,7], and large piezoelectricity was reported in monolayer Te_2Se [8] and monolayer MoSO [9]. Strong Dzyaloshinskii-Moriya interaction was found in Janus manganese dichalcogenides [10,11] and Janus chromium trihalides [12,13].

Since the electron affinity of S is lower than that of Se, there is electron accumulation on the S side of monolayer MoSSe, and consequently, monolayer MoSSe possesses an intrinsic out-of-plane electric dipole, pointing from S to Se. Multilayer MoSSe can have a potential buildup in the out-of-plane or z-direction if the electric dipoles of individual layers are aligned in the same direction. In this case, the band gap of multilayer MoSSe decreases with the number n of MoSSe layers, until it closes at $n = 4$ [17]. Since it is the intrinsic electric field that causes the band gap closing in four-layer MoSSe, we wondered whether the band gap can reopen upon application of a compensating external electric field. It is not a surprise, as we will show in the Results section (Sec. III), that a metal-to-semiconductor transition in four-layer MoSSe can be induced by an external out-of-plane electric field. Moreover, the critical electric field that is required to induce the metal-to-semiconductor transition in four-layer MoSSe is much smaller than that for a semiconductor-to-metal transition in bilayer MoS_2 [18]. In the context of a field-effect transistor, an external electric field can be applied via a dual gate configuration, whereas a single gate configuration induces electrostatic doping. We will also show how the electronic structure of four-layer MoSSe is affected by electrostatic doping. Furthermore, the internal electric field within four-layer MoSSe may allow rectification of an out-of-plane electric current, which sets another research goal of this study.

Guo and Dong [19] showed that the band gap of monolayer MoSSe can be significantly tuned by in-plane biaxial strain. Strain engineering of the electronic structure of heterogeneous bilayers MoSSe/WX_2 (X = S, Se) [20] and MoSSe/WSSe [21] has also been reported. These discoveries motivate us to investigate the influence of in-plane biaxial strain on the critical electric field for the metal-to-semiconductor transition. In

*hping@ufl.edu

Published by the American Physical Society under the terms of the Creative Commons Attribution 4.0 International license. Further distribution of this work must maintain attribution to the author(s) and the published article's title, journal citation, and DOI.

addition, we will also examine the influence of out-of-plane pressure on the critical electric field.

The rest of the paper is organized as follows. In Sec. II, we present the computational methods and simulation parameters. We then present our computational results in Sec. III, which is further divided into subsections concerning the atomic structure, external electric field, biaxial strain, rectifying effect, etc. Final conclusions are given in Sec. IV.

II. METHOD

Our calculations are based on density functional theory (DFT) [22,23] as implemented in the SIESTA package [24]. The effective screening medium (ESM) method is used to simulate the effects of out-of-plane electric field and electrostatic doping [25,26]. The DFT plus nonequilibrium Green's function (DFT + NEGF) method [27–29] is used to simulate electron transport properties of a Zr/four-layer MoSSe/Zr junction. We calculate the electron transmission and the electric current using the Caroli formula [30] and the Landauer formula [31,32], respectively.

We apply a double-ζ polarized (DZP) basis set [24] to expand the Kohn-Sham orbitals and the electron density. A mesh cutoff of 150 Ry is set to sample real space. A 15×15 Monkhorst-Pack k-point mesh [33] is chosen to sample the 2D reciprocal space for ionic relaxations. Ionic positions change by no more than 0.01 Å if we use a denser k-point mesh. Converging band energies usually require more k points than converging ion positions. For self-consistent calculations, the k-point mesh is increased to 21×21 such that the numerical error in energy bands is on the order of 1 meV. Electron transmission for our junctions as a function of k is highly oscillatory at certain energies, requiring many more k points to calculate the (k-)averaged electron transmission. In this situation, we increase the k-point mesh to 101×101 to obtain the averaged electron transmission, which then becomes smooth versus energy. The Fermi-Dirac distribution at $T = 300$ K is used to determine the occupation of electronic states. We adopt norm-conserving pseudopotentials as generated by the Troullier-Martins scheme [34] and the Perdew-Burke-Ernzerhof (PBE) exchange correlation energy functional [35]. The Van der Waals interaction is taken into account via the DFT-D2 method [36]. The atomic structure of four-layer MoSSe is fully optimized in all our calculations except for those under finite bias, since the atomic force under nonequilibrium conditions may not be reliable. The numerical tolerances for the density matrix, the Hamiltonian matrix, and the atomic force are no larger than 1×10^{-4}, 2×10^{-3} eV, and 0.02 eV/Å, respectively.

III. RESULTS

We present our results in seven parts. In Sec. III A, we first display our atomic structure of four-layer MoSSe. Next, in Sec. III B, we show a metal-to-semiconductor transition in four-layer MoSSe induced by an out-of-plane external electric field. Third is Sec. III C, in which we discuss the effects of electrostatic doping due to a single back gate. Fourth, we examine how the critical electric field for the metal-to-semiconductor transition is affected by in-plane biaxial strain in Sec. III D. Fifth, we discuss a sudden vertical compression of four-layer MoSSe due to a tensile in-plane strain in Sec. III E. Sixth, we demonstrate that four-layer MoSSe can rectify out-of-plane electric current in Sec. III F. Lastly, Sec. III G presents an odd-even effect on the electron transmission.

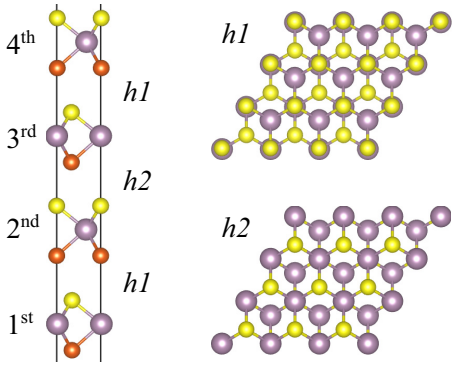


FIG. 1. Left: Side view of the four-layer MoSSe under study. Label $h1$ ($h2$) identifies a type 1 (type 2) hollow site interlayer stacking. Upper (lower) right: Top view of a bilayer MoSSe with $h1$ ($h2$) interlayer stacking. The color scheme is purple for Mo, yellow for S, and brown for Se.

A. Atomic structure

Our atomic structure of four-layer MoSSe is shown on the left side of Fig. 1. The S (Se) side of each MoSSe layer faces upward (downward). Adjacent MoSSe layers adopt a hollow site interlayer stacking, which is energetically more favorable than on-top site interlayer stacking [37,38]. There are two types of hollow site interlayer stacking, as shown on the right side in Fig. 1. Type 1 hollow site interlayer stacking ($h1$) is slightly higher in energy (by about 13 meV) than type 2 hollow site interlayer stacking ($h2$), which is consistent with previous studies [37,38]. In this work, we focus on the four-layer MoSSe with a stacking sequence of $h1$-$h2$-$h1$. The formation energy per interface $E_f = (E_{\text{four-layer}} - 4E_{\text{monolayer}})/3$ of this system is calculated to be -0.40 eV. Nevertheless, we additionally verify our major findings for $h1$-$h1$-$h1$ stacking four-layer MoSSe and $h2$-$h2$-$h2$ stacking four-layer MoSSe.

The structural properties of four-layer MoSSe with $h1$-$h2$-$h1$ stacking are summarized in Table I. The 2D Bravais lattice of four-layer MoSSe is hexagonal with a lattice constant of 3.347 Å, about 2.7% larger than that of monolayer MoSSe (not shown in the table). Our lattice constant for monolayer MoSSe is in good agreement with previous work [4,17]. The interlayer distance is measured between adjacent S and Se atomic layers. The distance between the third and the fourth MoSSe layers d_{34} is larger than d_{12} between the first and the second MoSSe layers, despite the same relative stacking. Such a difference in the interlayer distance is correlated with different local electronic structure in the top and the bottom layers (shown below in Sec. III B). The bond length $d_{\text{Mo-S}}$ is shorter than the bond length $d_{\text{Mo-Se}}$, indicating a stronger binding between Mo and S atoms. Both of these bond lengths vary by a marginal amount, within 0.01 Å, from

TABLE I. Structural properties of four-layer MoSSe with $h1$-$h2$-$h1$ stacking, as shown in Fig. 1. Entries a_1, a_2, and α are lattice parameters; d_{ij} is the interlayer distance between the ith and the jth MoSSe layers; $d_{\text{Mo-}X}$ (X = S, Se) is the length of the Mo-X bond; and $\angle X$-Mo-Y (X/Y = S, Se) is the angle between the Mo-X and the Mo-Y bonds.

a_1	a_2	α	d_{12}	d_{23}	d_{34}	$d_{\text{Mo-S}}$	$d_{\text{Mo-Se}}$	∠S-Mo-Se	∠S-Mo-S	∠Se-Mo-Se
3.35 Å	3.35 Å	60.0°	2.92 Å	2.94 Å	2.95 Å	2.46 Å	2.57 Å	79.6°	85.6°	81.3°

one MoSSe layer to another. The variation in the typical bond angles from layer to layer is within 0.1°.

B. Out-of-plane electric field

The inset of Fig. 2(a) illustrates our model setup for applying an out-of-plane electric field to four-layer MoSSe placed between two metal plates—a bottom gate and a top gate—separated by a distance L. The two gates have fixed electrostatic potentials, V_{BG} (V_{TG}), for the bottom (top) gate. Electric field in this work refers to the average electric field between the two gates,

$$E = (V_{\text{TG}} - V_{\text{BG}})/L. \tag{1}$$

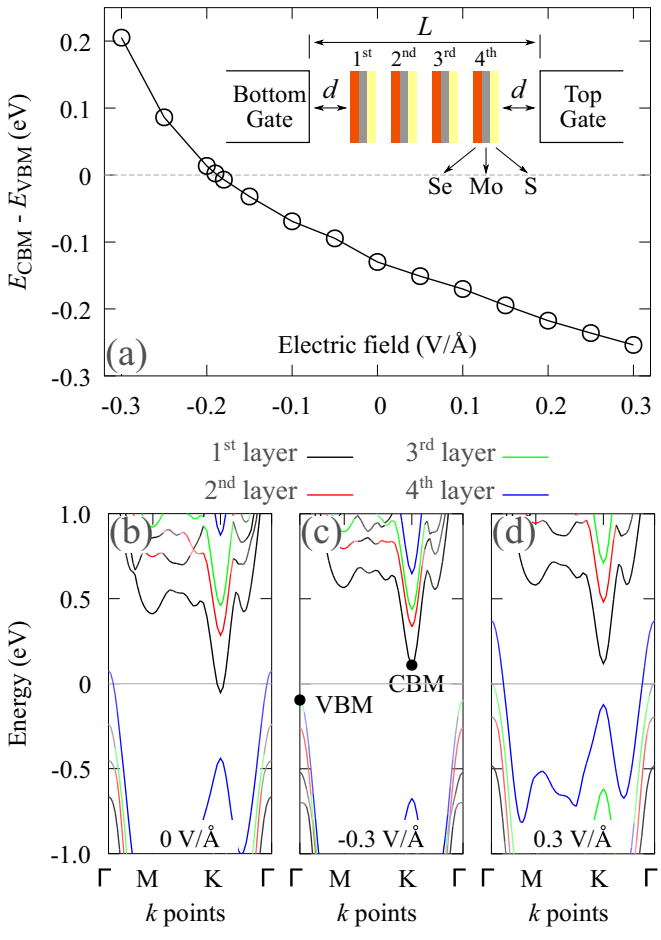


FIG. 2. (a) Energy difference between the CBM and the VBM of the four-layer MoSSe under different electric fields. The inset illustrates the system setup. (b)–(d) Band structures of four-layer MoSSe under zero, −0.30, and +0.30 V/Å electric fields, respectively. Colors identify the layer from which the band mainly originates (see the text). The CBM and VBM are marked in panel (c).

Each gate is spaced from the Janus MoSSe by a distance $d \sim 15$ Å of vacuum. The four MoSSe layers from bottom to top are labeled as first, second, third, and fourth layer, respectively. The sulfur side faces the top gate.

Figure 2(b) shows the band structure of the four-layer MoSSe under zero electric field. An energy band is colored black (red, green, blue) if it originates, roughly speaking, mainly from the first (second, third, fourth) layer. The details of the colormap are given in Appendix. There are two energy bands crossing the Fermi level, and thus the four-layer MoSSe is metallic. One band (black line) is the conduction band of the first layer [17] and crosses the Fermi level near the K point in the reciprocal space. The other band (blue line) is mainly the valence band of the fourth layer [17] and crosses the Fermi level near the Γ point in the reciprocal space. The first (fourth) layer gains (loses) electrons since its conduction (valence) band becomes partially occupied. If a negative electric field of −0.30 V/Å is applied, an energy gap of 0.20 eV opens up around the Fermi energy, and the four-layer MoSSe becomes a semiconductor [Fig. 2(c)]. In contrast, the four-layer MoSSe remains a metal if a positive electric field of +0.30 V/Å is applied [Fig. 2(d)]. To find the critical electric field for the metal-to-semiconductor transition, we examine the energy difference between the conduction-band minimum (CBM) and the valence-band maximum (VBM) versus electric field in Fig. 2(a). The energy difference $E_{\text{CBM}} - E_{\text{VBM}}$ decreases with electric field, and it reaches zero at a critical electric field of −0.187 V/Å.

These results were obtained for the four-layer MoSSe with $h1$-$h2$-$h1$ stacking. The critical electric field for the $h1$-$h1$-$h1$ and $h2$-$h2$-$h2$ stackings are −0.252 and −0.145 V/Å, respectively. Compared with the $h1$-$h2$-$h1$ stacking, the $h1$-$h1$-$h1$ ($h2$-$h2$-$h2$) stacking has a larger (smaller) critical field in magnitude. To understand such a difference, we analyze the internal potential buildup between adjacent MoSSe layers. Define $V(z)$ as the plane-averaged potential due to electrostatic interaction,

$$V(z) \equiv \frac{1}{A}\int_A [V_H(\boldsymbol{r}) + V_{\text{ion}}(\boldsymbol{r})]\, dx\, dy, \tag{2}$$

where V_H is the Hartree potential, V_{ion} is the ionic potential, and A is the area of a unit cell of the four-layer MoSSe. Denote the plane-averaged potential at the X (X = Se, S) atomic layer of the ith MoSSe layer as $V(z_{i,X})$. We find that the potential buildup, $V(z_{i+1,\text{Se}}) - V(z_{i,\text{S}})$, from the ith MoSSe layer to the $(i+1)$th MoSSe layer for $i = 1$, 2, and 3 is 1.39 eV ($h1$ stacking), 1.22 eV ($h2$ stacking), and 1.44 eV ($h1$ stacking), respectively. As such, the potential buildup between two MoSSe layers with $h1$ stacking is larger than that between two MoSSe layers with $h2$ stacking by about 0.2 eV. As a result, $h1$ stacking yields a stronger internal electric field, which then requires a larger external electric

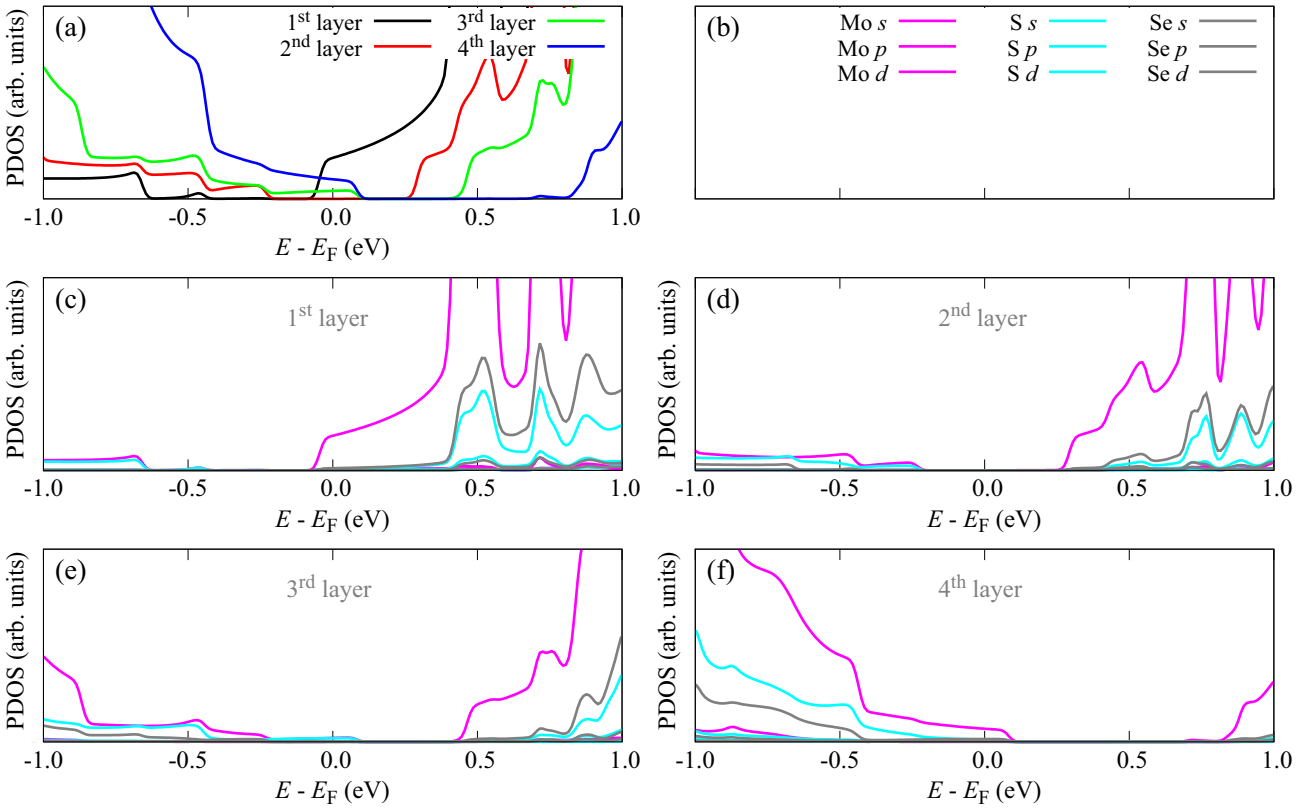


FIG. 3. (a) PDOS of each MoSSe layer. (b) Legend identifying curves in panels (c), (d), (e), and (f). (c)–(f) Orbital-decomposed PDOS for the first, second, third, and fourth MoSSe layers, respectively. The Fermi energy is set to zero.

field to compensate. Therefore, the critical electric field for the $h1$-$h1$-$h1$ ($h2$-$h2$-$h2$) stacking is larger (smaller) than that for the $h1$-$h2$-$h1$ stacking.

Figure 3(a) shows the layer-decomposed projected density of states (PDOS) for the four-layer MoSSe with $h1$-$h2$-$h1$ stacking under zero external electric field. The relative shift in energy of the four PDOS curves is due to the internal electric field. Recall that the four-layer MoSSe is metallic in such a way that both the valence and the conduction bands cross the Fermi energy. As seen from Fig. 3(a), the conduction-band states around the Fermi level originate solely from the first MoSSe layer, while the valence-band states around the Fermi level originate from both the third and fourth MoSSe layers. There are no states at the Fermi level originating from the second MoSSe layer. Furthermore, the PDOS of the fourth MoSSe layer is more than twice as large as the PDOS of the third MoSSe layer at the Fermi level. Therefore, the valence-band states around the Fermi level are mainly from the fourth MoSSe layer. Figures 3(c)–3(f) show the orbital-decomposed PDOS for the first, second, third, and fourth MoSSe layers, respectively. It is common for all four MoSSe layers that the states around the CBM are dominated by Mo d orbitals. For the states around the VBM of the first MoSSe layer, Mo d and S p orbitals have almost equal contributions. However, the states around the VBM of the fourth MoSSe layer originate mainly from Mo d orbitals. It appears that the fourth MoSSe layer loses S p electrons. Additional states occur within the band gap for the second and third MoSSe layers. These additional states mainly consist of Mo d and S p orbitals. The contribution from S and Se p orbitals to the valence (conduction) band becomes larger at lower (higher) energies. All other orbitals make a negligibly small contribution within the examined energy range.

C. Electrostatic doping

In the previous section, we have shown that a metal-to-semiconductor transition can be induced by an out-of-plane electric field when the system is charge-neutral. In this section, we examine the effects of electrostatic doping (charging) due to a back gate.

Figure 4(a) shows the energy difference between the CBM and the VBM versus doping level for the four-layer MoSSe with $h1$-$h2$-$h1$ stacking subject to a single back gate. An energy gap between the CBM and the VBM can be induced by electron (hole) doping if the S (Se) side of four-layer MoSSe faces the back gate. The gap-inducing external electric field for both Gate/$[\mathrm{S}-\mathrm{Mo}-\mathrm{Se}]_4$ (the S side faces the back gate) and Gate/$[\mathrm{Se}-\mathrm{Mo}-\mathrm{S}]_4$ (the Se side faces the back gate) is from the S side to the Se side of the four-layer MoSSe, in accordance with the results in the previous section. Figure 4(b) [Fig. 4(c)] shows the band structure of Gate/$[\mathrm{S}-\mathrm{Mo}-\mathrm{Se}]_4$ (Gate/$[\mathrm{Se}-\mathrm{Mo}-\mathrm{S}]_4$) at a doping level of -3.5 [$+3.5$] $\times 10^{13}$ cm^{-2}, as indicated by the dashed circles in Fig. 4(a). As seen from the figures, the conduction (valence) band still crosses the Fermi level, despite an energy gap between the CBM and the VBM. Therefore, electrostatic doping due to

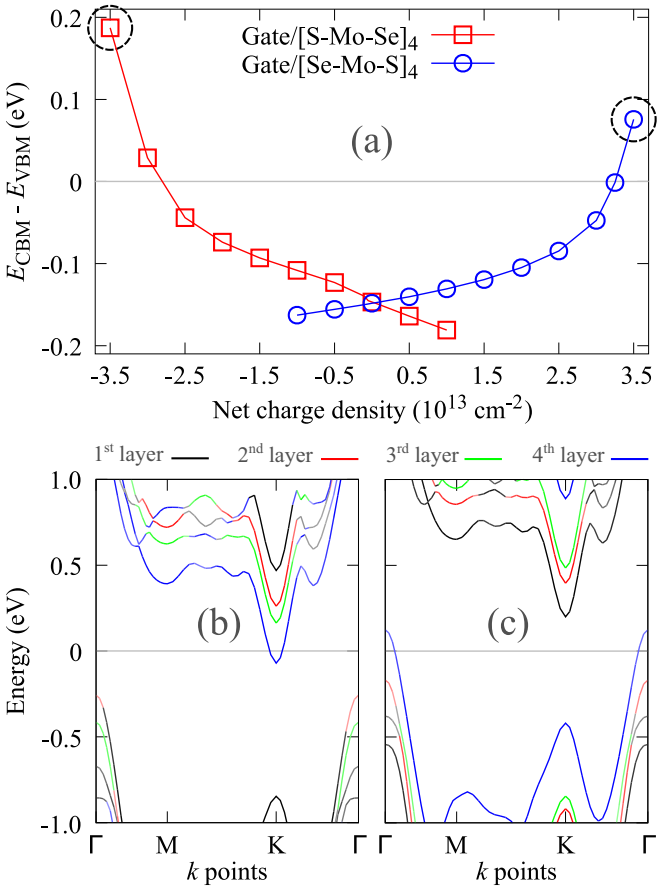


FIG. 4. (a) Energy difference between CBM and VBM. For red squares (blue circles) the S (Se) side of four-layer MoSSe faces the back gate. (b) [(c)] Energy bands of Gate/$[S-Mo-Se]_4$ [Gate/$[Se-Mo-S]_4$] under a doping level of -3.5 [$+3.5$] $\times 10^{13}$ cm^{-2} as indicated by the dashed circles in panel (a). Counting from the back gate, the four MoSSe layers are referred to as the first, second, third, and fourth layer, respectively.

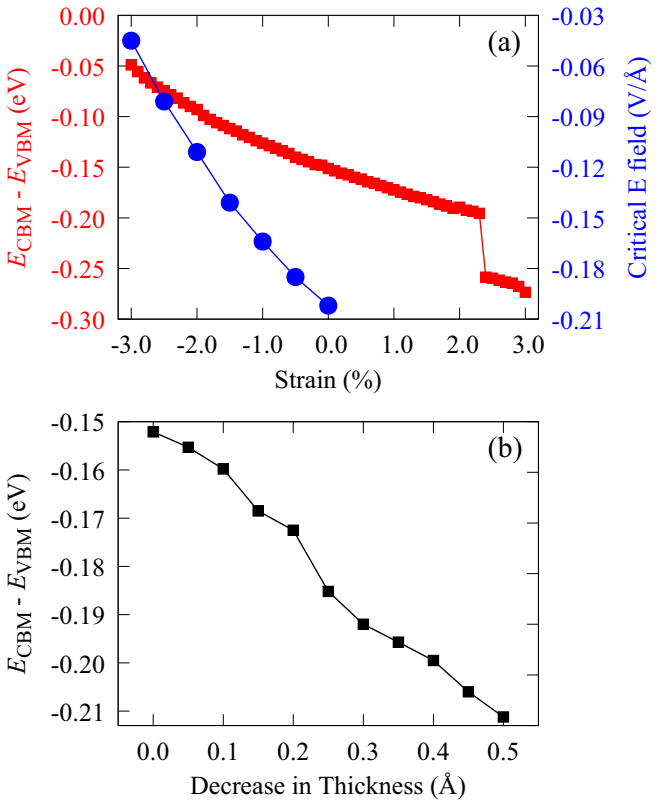


FIG. 5. (a) Shifts under strain: Red squares show the energy difference between the CBM and the VBM for four-layer MoSSe as a function of in-plane biaxial strain (left-hand scale). Blue circles show the critical electric field for the metal-to-semiconductor transition vs strain (right-hand scale). (b) Energy difference between the CBM and the VBM vs the thickness of four-layer MoSSe. Zero decrease corresponds to zero out-of-plane pressure, for which the thickness is 21.69 Å.

a single back gate does not induce a metal-to-semiconductor transition.

Figures 4(b) and 4(c) also show that the energy band that crosses the Fermi level originates from the fourth layer in both cases. Therefore, it is the fourth layer that conducts electric current at low temperatures after an energy gap (above the Fermi energy) opens upon doping. Note that the fourth MoSSe layer is farthest away from the back gate. This phenomenon may be useful for electronic devices in which delicate control of conducting channels is required.

D. Strain and pressure

The critical electric field of -0.187 V/Å is gigantic. In this section, we examine whether the critical field for the metal-to-semiconductor transition can be reduced by in-plane biaxial strain or out-of-plane pressure.

The red squares in Fig. 5(a) show the energy difference $E_{CBM} - E_{VBM}$ versus strain. The strain is measured by $(a - a_0)/a_0$, where a is the lattice constant under a finite strain and $a_0 = 3.347$ Å is the lattice constant under zero strain. A positive (negative) strain indicates tension (compression). Previously, Castellanos-Gomez *et al.* [39] applied a 2.5% tensile strain to few-layer MoS_2 in experiments. As MoSSe is a similar to MoS_2, in this work we consider strains within 3.0%, which should be relevant to experiments. According to our simulations, the stress at a 3.0% (-3.0%) strain is about 30 (38) kbar. $E_{CBM} - E_{VBM}$, which is always negative here, decreases (increases) with tensile (compressive) strain. Intuitively, a smaller $|E_{CBM} - E_{VBM}|$ would require a smaller electric field to open an energy gap between the CBM and the VBM. Therefore, we search for the critical electric field at several compressive strains, and we show the results as the blue circles in Fig. 5(a). Indeed, the magnitude of the critical field decreases with compressive strain. Under a compressive strain of -3.0%, the magnitude of the critical field is reduced to -0.045 V/Å, which is more feasible in experiments.

For the four-layer MoSSe with $h1$-$h1$-$h1$ stacking under a compressive strain of -3.0%, $E_{CBM} - E_{VBM}$ becomes -0.062 eV. The corresponding critical electric field is -0.112 V/Å, which is also significantly smaller in magnitude than the zero-strain value -0.252 V/Å for the same stacking. $E_{CBM} - E_{VBM}$ is approximately 0.007 eV for the four-layer MoSSe with $h2$-$h2$-$h2$ stacking under a compressive strain of -3.0%. A metal-to-semiconductor transition can be induced

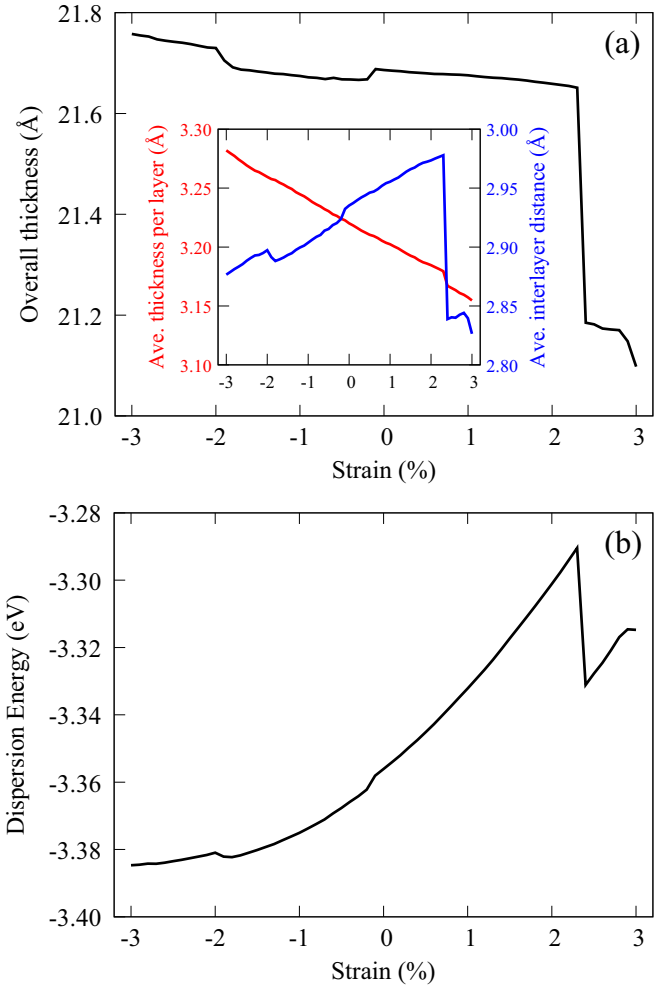


FIG. 6. (a) Thickness and (b) dispersion energy of four-layer MoSSe vs in-plane biaxial strain. Inset of (a): Average thickness per MoSSe layer and average interlayer distance vs in-plane biaxial strain.

by a moderate compressive strain alone for the $h2$-$h2$-$h2$ stacking. The critical in-plane biaxial strain is about −2.9%.

We additionally simulate out-of-plane pressure by reducing the thickness of the four-layer MoSSe with $h1$-$h2$-$h1$ stacking. All atoms are relaxed except the bottommost atomic layer and the topmost atomic layer. Our simulations show that $E_{\mathrm{CBM}} - E_{\mathrm{VBM}}$ decreases (becoming more negative) as the thickness is reduced; see Fig. 5(b). For example, a reduction in the thickness by 0.5 Å leads to a decreases in $E_{\mathrm{CBM}} - E_{\mathrm{VBM}}$ by about 0.06 eV. Thus, the critical electric field for a metal-to-semiconductor transition is likely to increase with out-of-plane pressure.

E. Abrupt structural change

As shown in Fig. 5(a), the energy difference $E_{\mathrm{CBM}} - E_{\mathrm{VBM}}$ exhibits a sudden decrease at a strain of ∼2.3%. This is accompanied by a sharp change in the thickness of the four-layer MoSSe. In this section, we investigate and explain this sharp structural change.

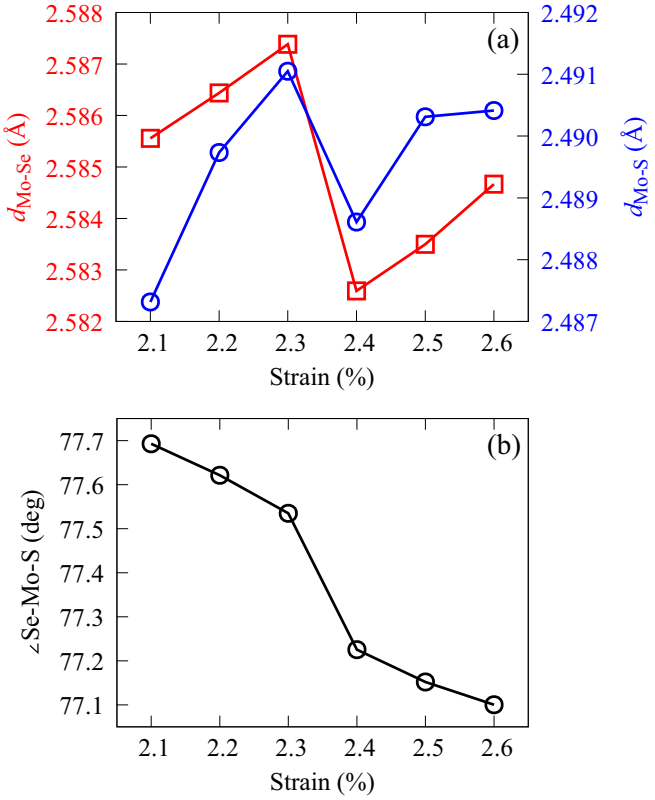


FIG. 7. (a) Bond lengths and (b) bond angle of the fourth MoSSe layer of four-layer MoSSe near the critical strain.

Figure 6(a) shows the overall thickness of four-layer MoSSe with $h1$-$h2$-$h1$ stacking versus in-plane biaxial strain. The thickness gradually decreases with tensile strain before a sharp decrease of 0.47 Å occurs at a strain of about ∼2.3%. This sharp decrease is a combined effect of abrupt decreases in both the interlayer distance and the thickness of individual MoSSe layers [see the inset of Fig. 6(a)]. As the strain increases from 2.3% to 2.4%, the change in the average interlayer distance is 0.139 Å, which is about 11 times larger than the change in the average thickness of individual MoSSe layers. Thus the sharp decrease in the overall thickness is dominated by the decrease in the interlayer distance. The reason for this sharp structural change is that it lowers the dispersion energy of the system [see Fig. 6(b)], as manifested in the sudden drop at a strain of ∼2.3%. It is worth mentioning that the function of total energy versus strain is smooth from −3.0% to 3.0%.

To reveal the changes in bond length and bond angle within a MoSSe monolayer, we choose the fourth MoSSe layer as a representative. As shown in Fig. 7(a), both the Mo-Se and Mo-S bond lengths $d_{\mathrm{Mo\text{-}Se}}$ and $d_{\mathrm{Mo\text{-}S}}$ increase with strain before (strain $< 2.3\%$) and after (strain $> 2.4\%$) the sharp decrease in the overall thickness of the four-layer MoSSe. However, $d_{\mathrm{Mo\text{-}Se}}$ ($d_{\mathrm{Mo\text{-}S}}$) decreases by about 0.005 Å (0.003 Å) as the strain increases from 2.3% to 2.4%. Figure 7(b) shows the bond angle ∠Se-Mo-S versus the strain. The bond angle always decreases with strain, and the rate of decrease is slightly faster for $2.3\% \leqslant$ strain $\leqslant 2.4\%$. The reduction of the Mo-Se and Mo-S bond lengths together with a faster decrease in

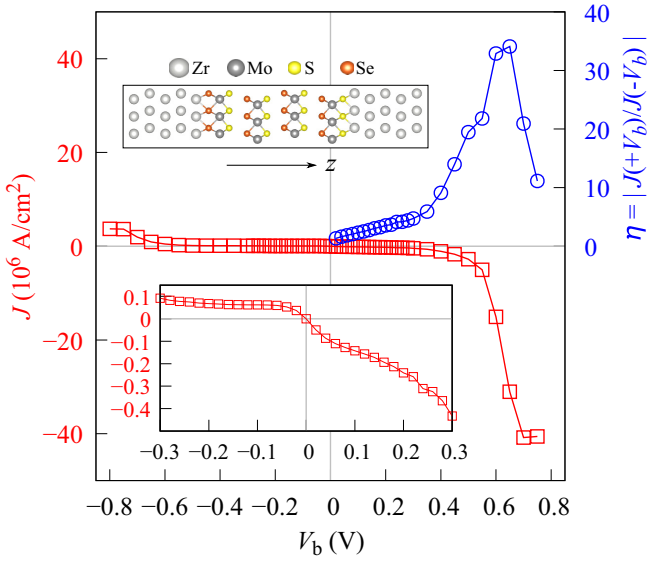


FIG. 8. Red squares show the electric current density in a Zr/four-layer MoSSe/Zr junction as a function of bias voltage. Blue circles show the rectifying ratio of the junction vs bias voltage. The inset zooms in on the central part of the junction.

the bond angle ∠Se-Mo-S signify the sharp decrease of the thickness of a MoSSe monolayer.

F. Rectifying effect

Since four-layer MoSSe has a substantial internal electric field, we suspect it may rectify out-of-plane electric current when employed in a circuit. Here, we present a proof-of-concept calculation where the four-layer MoSSe with $h1$-$h2$-$h1$ stacking is sandwiched between two zirconium electrodes, as shown in the upper inset of Fig. 8. The Zr electrode is chosen due to a relatively small lattice mismatch of ∼3% (∼1%), with four-layer (monolayer) MoSSe. In actual experiments, one might need high vacuum to prevent a Zr surface from oxidation by oxygen molecules in the air. The Zr/four-layer MoSS/Zr junction is periodic in the x- and y-directions, and electron transport is along the z-direction. Although only two finite pieces of Zr are shown in the inset of Fig. 8, the model left and right electrodes extend to infinity, which is standard in the DFT + NEGF method [27].

The red squares in Fig. 8 show the calculated electric current density J in the Zr/four-layer MoSS/Zr junction as a function of bias voltage V_b, defined by

$$V_b = \mu_L - \mu_R, \tag{3}$$

where μ_L (μ_R) is the chemical potential of the left (right) electrode. The electric current density J is calculated by the Landauer formula [31,32],

$$J = \frac{2e}{hA}\int_{-\infty}^{\infty} dE\,[f_L(E) - f_R(E)]\,T(E), \tag{4}$$

where e is the elementary charge, h is the Planck constant, A is the area of a unit cell, and f_L and f_R are the Fermi-Dirac distribution functions for the left and right electrodes. The

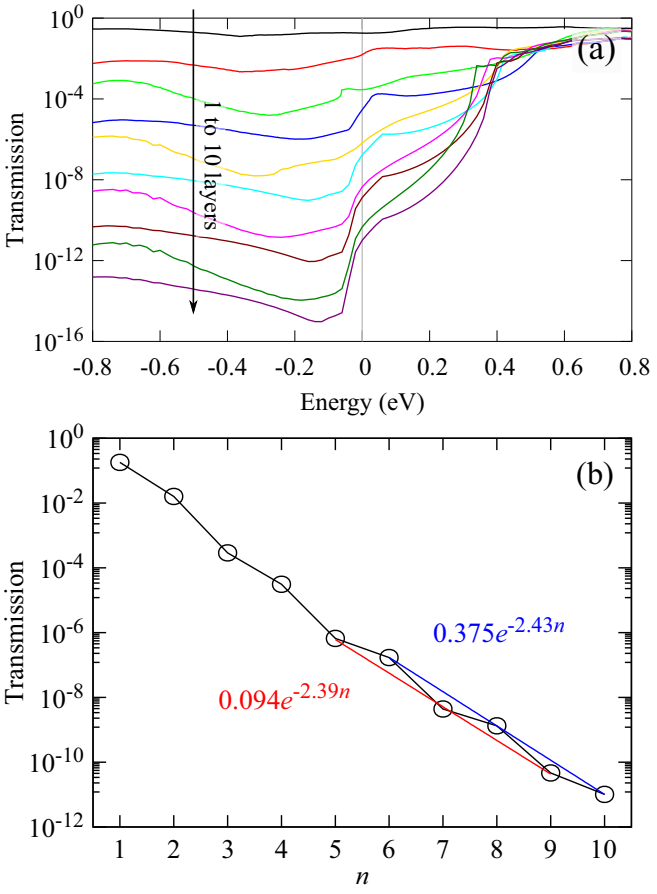


FIG. 9. (a) Electron transmission vs energy for Zr/n-layer MoSSe/Zr junctions with $n = 1, 2, 3, \ldots, 10$. The Fermi energy is set to zero. (b) Electron transmission at the Fermi energy for Zr/n-layer MoSSe/Zr junctions vs the number of layers n.

electron transmission function $T(E)$ is calculated as

$$T(E) = \mathrm{Tr}\,\{\mathbf{\Gamma}_L(E)\mathbf{G}^{\mathrm{r}}(E)\mathbf{\Gamma}_R(E)\mathbf{G}^{\mathrm{a}}(E)\}, \tag{5}$$

where $\mathbf{\Gamma}_L$ ($\mathbf{\Gamma}_R$) is the level width function of the left (right) electrode, and $\mathbf{G}^{\mathrm{r}}$ ($\mathbf{G}^{\mathrm{a}}$) is the retarded (advanced) Green's function. A zoom of the J-V_b curve at low bias voltages is shown in the lower inset. $J(-0.02\ \mathrm{V})$ is about 3.7×10^4 A/cm^2, which is of the same order as $J(+0.02\ \mathrm{V}) \sim -5.0 \times 10^4$ A/cm^2. Defining a rectifying ratio η as

$$\eta = |J(+V_b)/J(-V_b)|, \tag{6}$$

we see that $\eta(0.02\ \mathrm{V})$ is as small as 1.4. As shown by the blue circles in Fig. 8, η first gradually increases with bias voltage, reaching 4.7 at 0.3 V. But, as the bias voltage further increases in the positive direction, a sharp increase in the electric current density occurs at around +0.6 V. With no such sharp increase at negative bias voltages, a rectifying ratio as high as 34.1 is achieved at 0.65 V, after which η begins to decrease, falling to 11.1 at 0.75 V.

We next examine whether the rectifying ratio can be enhanced by tuning the number of MoSSe layers. Figure 9(a) shows electron transmission as a function of energy $T_n(E)$ for Zr/n-layer MoSSe/Zr junctions under zero bias with $n =$

1, 2, 3, . . . , 10. Setting the Fermi energy to zero, we observe that $T_n(E)$ decays exponentially with n for $E \in [-0.8 : 0]$ eV. In particular, $T_{10}(E)$ is more than 10 orders of magnitude smaller than $T_1(E)$ within this energy range. In contrast, $T_n(E)$ is always above 10^{-2} (and smaller than 1) regardless of n for $E \in [0.5 : 0.8]$ eV. Thus, we infer from the zero bias transmission function that thicker MoSSe should exhibit a higher rectifying ratio. We verify this idea using a Zr/five-layer MoSSe/Zr junction, and we obtain the higher value $\eta = 85.6$ at $V_b = 5.5$ V.

G. Odd-even effect

Figure 9(b) shows the electron transmission at the Fermi energy $T_n(E_F)$ for Zr/n-layer MoSSe/Zr junctions under zero bias with $n = 1, 2, 3, \ldots, 10$. For simplicity, we will write $T_n(E_F)$ as T_n in the rest of this section. As seen from the figure, T_n decays differently for even n and odd n. When $n \geqslant 5$, T_n can be well fit by a function of the form $T_n = \lambda e^{-\gamma n}$, where γ signifies the limiting decaying rate of evanescent states at the Fermi level. The physical meaning of λ is vague, and we just use it as a fitting parameter here. The fitted functions are $T_n^{\rm o} \approx 9.44 \times 10^{-2}\, e^{-2.39n}$ for odd n and $T_n^{\rm e} \approx 3.75 \times 10^{-1}\, e^{-2.43n}$ for even n [see Fig. 9(b)]. The values $\gamma^{\rm o} = 2.39$ and $\gamma^{\rm e} = 2.43$ are close to each other, indicating that the evanescent states in odd and even junctions have similar limiting decaying rates. This is reasonable since evanescent states are determined by bulk properties rather than interface properties. In contrast, the overall amplitude $\lambda^{\rm o} = 9.44 \times 10^{-2}$ is about four times smaller than $\lambda^{\rm e} = 3.75 \times 10^{-1}$. Interpolating, we see that $T_n^{\rm o} < T_n^{\rm e}$ at the same value of n ($6 \leqslant n \leqslant 9$). As we argue below, such a difference in the electron transmission between odd and even junctions can be explained by parity-dependent interface properties.

The contact between the left Zr electrode and the n-layer MoSSe is the same for all junctions, while the contact on the right side is different for even and odd junctions, as depicted in Figs. 10(a) and 10(b). As a consequence, there is a parity-dependent potential difference between the adjacent Zr and S atomic layers as shown in Fig. 10(c). For $n \geqslant 5$, the odd junctions possess an ∼0.25 eV higher potential difference $V_{\rm Zr} - V_{\rm S}$ than the even junctions. Therefore, the interpolated electron transmission $T_n^{\rm o}$ is smaller than the interpolated $T_n^{\rm e}$ at the same value of n. It is worth mentioning that the number of electrons at the right contact also exhibit an oscillatory behavior for $n \geqslant 5$, as shown in Fig. 11: there are more electrons accumulated at the right contact in even junctions than in odd junctions. Due to Coulomb repulsion, the interface with more electrons tends to present a higher energy barrier.

IV. CONCLUSION

We have performed a detailed study of the electronic and electron transport properties of n-layer MoSSe ($n = 1$–10) with a focus on $n = 4$ using first-principles-based density functional theory. Several significant findings were obtained: (i) We show that a metal to semiconductor transition can be induced by an out-of-plane electric field. (ii) Sensitive to the stacking order, the critical electric fields for the four-layer MoSSe with $h1$-$h1$-$h1$, $h1$-$h2$-$h1$, and $h2$-$h2$-$h2$ stackings are,

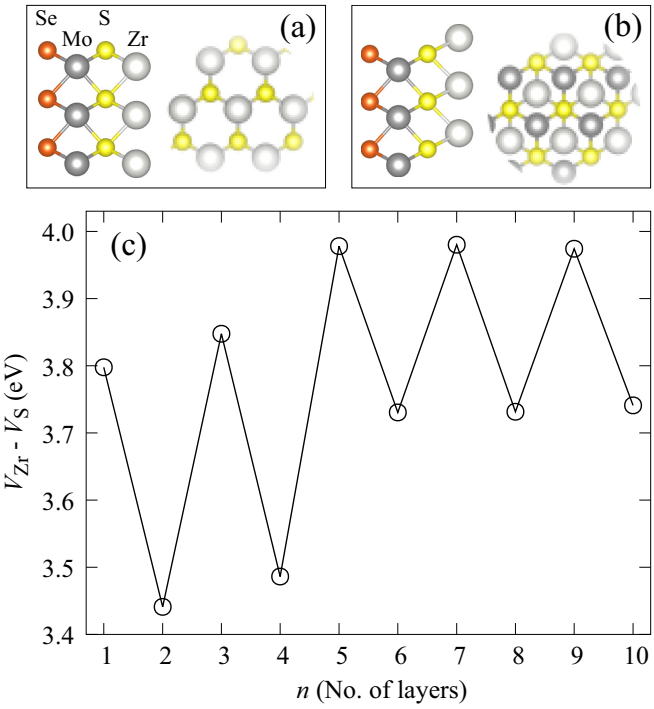


FIG. 10. (a) [(b)] Top and side views of the contact between MoSSe and Zr on the right side of Zr/n-layer MoSSe/Zr junctions with n being odd [even]. (c) Difference between the plane averaged electrostatic potential at Zr and that at S at the contact shown in panels (a) and (b).

respectively, −0.252, −0.187, and −0.145 V/Å. (iii) The critical electric field for the $h1$-$h1$-$h1$ stacking is highest (in magnitude) because the internal potential buildup with $h1$ stacking is larger than that with $h2$ stacking. We can reduce the critical electric field by applying an in-plane biaxial compressive strain, and this works for all three stackings. (iv) The applied strain induces a second phase transition, indicated by a sudden compression in the vertical dimension. (v) The four-layer MoSSe with $h1$-$h2$-$h1$ stacking is always metallic upon electrostatic doping, although an energy gap between the conduction minimum and the valence maximum can be

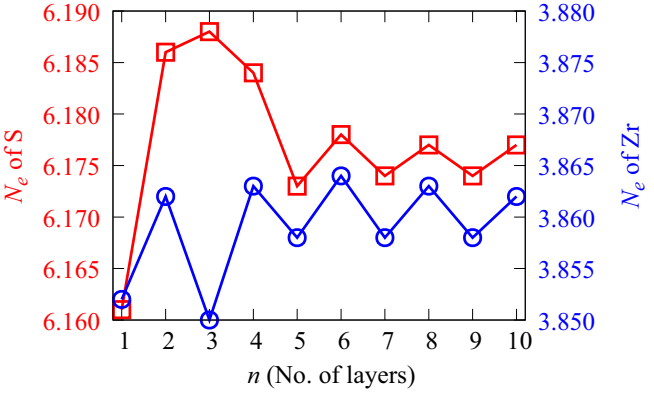


FIG. 11. Mulliken charge analysis: the number of electrons per S or Zr atom at the right contact of Zr/n-layer MoSSe/Zr junctions vs the number of MoSSe layers n.

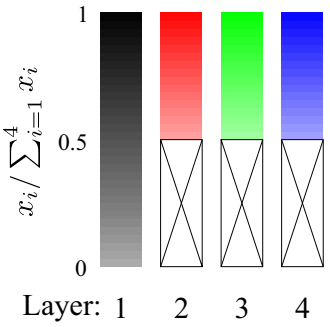


FIG. 12. Colormap of the relative projected density of states (PDOS) from each MoSSe layer. x_i represents the PDOS from the ith layer.

opened. (vi) When sandwiched between two Zr electrodes, the four-layer MoSSe can rectify electric current with a maximum rectifying ratio of 34.1 at 0.65 V. (vii) The rectifying ratio can be enhanced by increasing the number of MoSSe layers. Concluded from a high-level computational approach, these results have predictive power, and one can use a combination of these controlling parameters to guide future experiments in areas of material design and nanoelectronics. For example, due to the metal-to-semiconductor transition, four-layer MoSSe can be applied in electrical switches.

ACKNOWLEDGMENTS

This work is supported by the U.S. Department of Energy (DOE), Office of Basic Energy Sciences (BES), under Contract No. DE-FG02-02ER45995. Computations were performed using the utilities of National Energy Research Scientific Computing Center and University of Florida Research Computing.

APPENDIX: COLORMAP FOR FIG. 2

Figure 12 shows the colormap for Fig. 2 in the main text. It is generated using the following script for GNUPLOT.

```
set palette model RGB
set palette color
set palette defined(\
0.0"#aaaaaa", 0.2"#808080", 1.0"#000000", \
1.1"#ffffff", 1.2"#ffffff", 2.0"#ff0000", \
2.1"#ffffff", 2.2"#ffffff", 3.0"#00ff00", \
3.1"#ffffff", 3.2"#ffffff", 4.0"#0000ff")

g(x1, x2, x3, x4) = \
x1/(x1 + x2 + x3 + x4) > 0.5?x1/(x1 + x2 + x3 + x4) : \
x2/(x1 + x2 + x3 + x4) > 0.5?x2/(x1 + x2 + x3 + x4) + 1 : \
x3/(x1 + x2 + x3 + x4) > 0.5?x3/(x1 + x2 + x3 + x4) + 2 : \
x4/(x1 + x2 + x3 + x4) > 0.5?x4/(x1 + x2 + x3 + x4) + 3 : \
x1/(x1 + x2 + x3 + x4)

p "bands.dat" u 1:2:g($3, $4, $5, $6) w l palette
```

In this script, x_i is the projected density of states (PDOS) of the ith MoSSe layer due to a Kohn-Sham state. If the ratio $\tau_i = x_i/(x_1 + x_2 + x_3 + x_4)$ is greater than 0.5, then the contribution from the ith layer dominates. We identify the dominant layer index by color type (black, red, green, or blue), and we represent the value of τ_i by color brightness. If none of τ_i ($i = 1, 2, 3, 4$) is greater than 0.5, then we use a grayscale according to the value of τ_1.

[1] B. Radisavljevic, A. Radenovic, J. Brivio, V. Giacometti, and A. Kis, Nat. Nanotechnol. **6**, 147 (2011).
[2] D. Lembke, S. Bertolazzi, and A. Kis, Acc. Chem. Res. **48**, 100 (2015).
[3] F. A. Rasmussen and K. S. Thygesen, J. Phys. Chem. C **119**, 13169 (2015).
[4] J. Zhang, S. Jia, I. Kholmanov, L. Dong, D. Q. Er, W. B. Chen, H. Guo, Z. H. Jin, V. B. Shenoy, L. Shi, and J. Lou, ACS Nano **11**, 8192 (2017).
[5] A. Y. Lu, H. Y. Zhu, J. Xiao, C. P. Chuu, Y. M. Han, M. H. Chiu, C. C. Cheng, C. W. Yang, K. H. Wei, Y. M. Yang, Y. Wang, D. Sokaras, D. Nordlund, P. D. Yang, D. A. Muller, M. Y. Chou, X. Zhang, and L. J. Li, Nat. Nanotechnol. **12**, 744 (2017).
[6] J. Wang, H. B. Shu, T. F. Zhao, P. Liang, N. Wang, D. Cao, and X. S. Chen, Phys. Chem. Chem. Phys. **20**, 18571 (2018).
[7] C. X. Xia, W. Q. Xiong, J. Du, T. X. Wang, Y. T. Peng, and J. B. Li, Phys. Rev. B **98**, 165424 (2018).
[8] Y. Chen, J. Y. Liu, J. B. Yu, Y. G. Guo, and Q. Sun, Phys. Chem. Chem. Phys. **21**, 1207 (2019).
[9] M. Yagmurcukardes and F. M. Peeters, Phys. Rev. B **101**, 155205 (2020).
[10] J. R. Yuan, Y. M. Yang, Y. Q. Cai, Y. H. Wu, Y. P. Chen, X. H. Yan, and L. Shen, Phys. Rev. B **101**, 094420 (2020).
[11] J. Liang, W. Wang, H. Du, A. Hallal, K. Garcia, M. Chshiev, A. Fert, and H. Yang, Phys. Rev. B **101**, 184401 (2020).
[12] C. S. Xu, J. S. Feng, S. Prokhorenko, Y. Nahas, H. J. Xiang, and L. Bellaiche, Phys. Rev. B **101**, 060404(R) (2020).
[13] F. Zhang, H. Zhang, W. B. Mi, and X. C. Wang, Phys. Chem. Chem. Phys. **22**, 8647 (2020).
[14] C. M. Zhang, Y. H. Nie, S. Sanvito, and A. J. Du, Nano Lett. **19**, 1366 (2019).
[15] H. R. Jappor, M. M. Obeid, T. V. Vu, D. M. Hoat, H. D. Bui, N. N. Hieu, S. J. Edrees, Y. Mogulkoc, and R. Khenata, Superlattices Microstruct. **130**, 545 (2019).
[16] F. Zhang, W. B. Mi, and X. C. Wang, Adv. Electron. Mater. **6**, 1900778 (2020).
[17] A. C. Riis-Jensen, M. Pandey, and K. S. Thygesen, J. Phys. Chem. C **122**, 24520 (2018).
[18] Q. H. Liu, L. Z. Li, Y. F. Li, Z. X. Gao, Z. F. Chen, and J. Lu, J. Phys. Chem. C **116**, 21556 (2012).
[19] S. D. Guo and J. Dong, Semicond. Sci. Technol. **33**, 085003 (2018).
[20] C. Yu and Z. G. Wang, Phys. Status Solidi B **256**, 1900261 (2019).
[21] W. Y. Guo, X. Ge, S. T. Sun, Y. Q. Xie, and X. Ye, Phys. Chem. Chem. Phys. **22**, 4946 (2020).
[22] P. Hohenberg and W. Kohn, Phys. Rev. **136**, B864 (1964).

[23] W. Kohn and L. J. Sham, Phys. Rev. **140**, A1133 (1965).
[24] J. M. Soler, E. Artacho, J. D. Gale, A. Garcia, J. Junquera, P. Ordejon, and D. Sanchez-Portal, J. Phys.: Condens. Matter **14**, 2745 (2002).
[25] M. Otani and O. Sugino, Phys. Rev. B **73**, 115407 (2006).
[26] H.-P. Cheng, S. Liu, X. Chen, L. Zhang, and J. N. Fry, AVS Quantum Sci. **2**, 027101 (2020).
[27] J. Taylor, H. Guo, and J. Wang, Phys. Rev. B **63**, 121104(R) (2001).
[28] Y. Q. Xue, S. Datta, and M. A. Ratner, Chem. Phys. **281**, 151 (2002).
[29] M. Brandbyge, J. L. Mozos, P. Ordejon, J. Taylor, and K. Stokbro, Phys. Rev. B **65**, 165401 (2002).
[30] C. Caroli, R. Combescot, P. Nozieres, and D. Saint-James, J. Phys. C **4**, 916 (1971).
[31] R. Landauer, IBM J. Res. Dev. **1**, 223 (1957).
[32] R. Landauer, Philos. Mag. **21**, 863 (1970).
[33] H. J. Monkhorst and J. D. Pack, Phys. Rev. B **13**, 5188 (1976).
[34] N. Troullier and J. L. Martins, Phys. Rev. B **43**, 1993 (1991).
[35] J. P. Perdew, K. Burke, and M. Ernzerhof, Phys. Rev. Lett. **77**, 3865 (1996).
[36] S. Grimme, J. Comput. Chem. **27**, 1787 (2006).
[37] W. J. Yin, B. Wen, G. Z. Nie, X. L. Wei, and L. M. Liu, J. Mater. Chem. C **6**, 1693 (2018).
[38] Z. Y. Guan, S. Ni, and S. L. Hu, J. Phys. Chem. C **122**, 6209 (2018).
[39] A. Castellanos-Gomez, R. Roldán, E. Cappelluti, M. Buscema, F. Guinea, H. S. J. van der Zant, and G. A. Steele, Nano Lett. **13**, 5361 (2013).